Computational Analysis of Rheological Secondary Flow in a Pipe-Manifold Containing In-Plane Double Bends

A. Banerjee[1, 2], S. Sengupta[1†] and S. Pramanik[1]

[1]*Department of Mechanical Engineering, National Institute of Technology, Durgapur, 713209 (W.B.), India*
[2]*Department of Mechanical Engineering, Dr. B. C. Roy Engineering College, Durgapur- 713206 (W.B.), India*

†*Corresponding Author Email:sayantan.sengupta@me.nitdgp.ac.in*

ABSTRACT

Non-Newtonian fluid flow in pipe bends is inevitable in industrial applications. Previous researchers have extensively explored Newtonian flow through curved ducts. However, the non-Newtonian counterpart gets little attention. We study the turbulent flow of shear-dependent fluids obeying the Power-Law model in a pipe manifold containing an in-plane double bend. Ostwald–de Waele's power law is used to model the fluid's rheology. We utilize computational fluid dynamics (CFD) to solve Reynolds-averaged Navier–Stokes (RANS) equations with the k-ε turbulence model. We validate our numerical results with previous experimental results. The in-plane double bend perturbs the flow in the pipe manifold to develop a Prandtl's secondary flow of the first kind. A fully developed flow at the bend upstream is disturbed due to the bend's curvature and regains its fully developed characteristics upon a certain downstream length after the exit of the bend. We study the rheological characteristics of the secondary flow within the bend and the evolution of fluid flow at the bend downstream. We demonstrate that the centrifugal force-dominated secondary flow increases with a decrease of the non-Newtonian power-law index. We capture the camel's-back-shaped velocity profiles within the bend due to accelerating-decelerating flow. The study reveals that the average flow velocity increases along the bend with a corresponding pressure head loss. We quantify this velocity rise by a newly introduced non-dimensional number, viz. enhancement ratio. The double bend's enhancement ratio decreases with an increase in *n*.

1. INTRODUCTION

Bent pipes are unavoidable in industries like gas and oil, food processing, paper manufacturing, and heat & energy sectors like nuclear power plants, solar thermal systems etc. The evolution of cross-stream flow inside a skewed pipe, i.e. Prandtl's secondary flow of the first kind, has been a matter of concern for years (Bradshaw et al., 1987; Lai et al., 1991; Kalpakli et al., 2016). Additional losses are incurred in the pressure head due to the presence of bends in ducts (Ito 1960), which is a matter of concern for engineers to optimize energy consumption. This loss is due to the disturbances created by cross-stream flow, which is greatly affected by both the Reynolds number (*Re*) and curvature ratio (Berger et al., 1983; Ito 1987). The curvature ratio is a geometrical parameter, defined as the ratio of bend radius to the inner radius of the pipe, i.e. R_c/R. A non-dimensional number called Dean number

(*De*) defined as, $De \equiv Re\sqrt{R_c/R}$; is often used to characterize the effect of *Re* and (R_c/R) on flow inside curved pipes in a combined manner. On the contrary, analyzing the individual effect of *Re* and R_c/R is a good practice in many cases, such as turbulent flows (Cieślicki & Piechna, 2012; Canton et al., 2016). Prandtl's secondary flow of the first kind is always a centrifugal-force dominated flow, resulting in a local pressure gradient (Barua 1963) which causes the mid-plane fluid particles to move towards the outer core of the pipe along with the formation of a pair of counter-rotating Dean vortices (Dean, 1927).

Effective space utilization is a matter of concern in industries, attracting engineers towards layout complexity while designing a system. To avoid long-distance straight pipes, often bends and bend-combinations are employed. Successive bends or bend combinations may be either in-

NOMENCLATURE			
CFD	Computational Fluid Dynamics	n	power law index
D	inner diameter of the pipe	V_i	bulk velocity at inlet
$\boldsymbol{D}$	rate of deformation tensor	V_p	magnitude of primary velocity
De	Dean number	V_s	magnitude of secondary velocity
K	consistency index	ε	rate of dissipation of the turbulent kinetic energy
k	turbulent kinetic energy	ϵ	enhancement ratio
L_s	length of straight upstream section	φ	non-dimensional pressure difference
L_b	length of bend section	μ	viscosity
L_d	length of downstream section	μ_w	viscosity at wall
R	inner Radius of the pipe	τ	shear stress
R_c	radius of curvature of the pipe bend	$\dot{\gamma}$	rate of shear strain
Re	Reynolds number		

plane or out-of-plane types. These bends are the sources of additional turbulence distortions (Aichouni et al., 2016). Very few studies are available on flow through different bend conditions, e.g. Fiedler 1997, Laribi et al. 2010, 2013, Shwin et al. 2017, out of which most literature concentrated on out-of-plane bend combinations. Turbulent flow in out-of-plane double bend is a lucid area in Fluid dynamics. Fiedler 1997 theoretically explained the flow physics in an out-of-plane (90º) double bend. A detailed experimental study was performed by Xiong et al. 2003. Straka et al. 2019 examined the effect of swirl in the out-of-plane (90º) double bend. We, however, focus on the local flow behaviors of an in-plane (90º) double bend.

Dense power plant slurry, fruit juices, paper pulp, various materials in the pharmaceutical industry, wastewater, and crude oil are some popular non-Newtonian fluids in engineering applications. With the increasing usage of non-Newtonian fluids, it has been an obvious requirement to study the flow behaviors of these fluids through bends in order to operate their flows most economically. Several studies to investigate bend losses for non-Newtonian fluids have been made. Polizelli et al. (2003) focused on friction losses in valves and fittings for these fluids. Bíbok et al. (2020) studied pressure drops and flow patterns of two real power law fluids passing through a 90º elbow, both experimentally and numerically. Although previous studies on non-Newtonian fluid flow in bend are not extensive, several attempts have been made to understand the flow behaviors for different applications, such as dense slurry mixtures (Csizmadia, 2016; Singh et al., 2019), power plant slurries (Csizmadia & Hős, 2013), liquid food products (Cabral et al., 2011) and liquid eggs (Yigit et al., 2016). Some other works may also be mentioned exploring various flow features of power-law fluids in a stationary duct (Lambride et al., 2023) and adjacent to rotating ducts (Khali et al., 2017, 2022, Khali & Nebbali, 2023). Non-Newtonian power-law behaviors of nano-fluids are also seeking the interests of recent researchers [Esfe & Rostamian, (2017), Ellahi et al. (2019), Dey & Mahanta (2022)]. It is well known that for all incompressible Newtonian fluids, shear stress ($\boldsymbol{\tau}$) is proportional to the rate of deformation tensor ($\boldsymbol{D}$),

$$\boldsymbol{\tau} = \mu \boldsymbol{D} \tag{1}$$

where, $\boldsymbol{D} = \left(\dfrac{\partial u_j}{\partial u_i} + \dfrac{\partial u_i}{\partial u_j}\right) \tag{2}$

The viscosity, μ is independent of $\boldsymbol{D}$ for Newtonian fluids. However, for non-Newtonian fluids, it is a function of the rate of shear strain, $\dot{\gamma}$ related to $\boldsymbol{D}$ as follows:

$$\dot{\gamma} = \sqrt{\frac{1}{2} \boldsymbol{D} : \boldsymbol{D}} \tag{3}$$

where, $\boldsymbol{D} : \boldsymbol{D}$ represents Frobenius product of $\boldsymbol{D}$.

After carefully reviewing prior literature, the authors found that studies of turbulent flow through in-plane 90° double bends could be more extensive. Such studies with non-Newtonian fluids are never reported heretofore. Our study utilizes the power-law model for the rheological characterization of viscoplastic non-Newtonian fluids. Viscoplastic fluids are materials which behave like a rigid body and undergo modest deformation as long as the exerted shear stress does not exceed a yield stress limit; beyond the threshold, they behave like a viscous fluid (Mitsoulis 2007). A few examples of viscoplastic fluids are as follows: drilling muds, crude oils extracted in petroleum industries, fruit juices, egg yolk, and starch from the food industry, sewage slurry, toothpaste, paints, dairy products and many more. A well-known model for characterizing viscoplastic fluids' behavior is the Herschel-Bulkley model (Mendes & Dutra, 2004), which is written as:

$$\begin{cases} \tau = \tau_0 + K\dot{\gamma}^n, when, \tau > \tau_0 \\ else, \dot{\gamma} = 0 \end{cases} \tag{4}$$

where, τ is the shear stress, K is the consistency index, τ_0 is the yield stress, and n is the flow behavior index. This equation would reduce to Ostwald–De Waele power law model (Shapovalov 2017) if τ_0 is considered to be zero.

$$\tau = K\dot{\gamma}^n \tag{5}$$

Fluids obeying this particular model are known as power-law fluids. Power law fluids, which are mainly classified into shear-thinning (power law index, $n < 1$) and shear-thickening ($n > 1$), are generally considered within a range of n from 0.6 to 1.8 (Yigit et al., 2016). Corn starch and water mixes, silly putty, and sand in water are some examples of shear-thickening fluids, on the other hand, ketchup, paint, glue, and blood exhibit shear-thinning behavior. Unlike the power-law model, the tangent hyperbolic fluid model (Chu et al., 2023) is often used to characterize polymeric shear-thinning fluids. The

Casson model (Li et al., 2023a) is attributed to shear-thinning fluids having finite yield stress. The Carreau model (Li et al., 2023b) is used for fluids which exhibit shear-thinning behavior at a low shear rate and shear-thickening behavior at a higher shear rate.

It is challenging to come up with a unique definition of the Reynolds number, which may appropriately characterize a non-Newtonian fluid flow. The present authors find many definitions of the Reynolds number in the existing literature utilized by previous researchers. Typically, Reynolds numbers for non-Newtonian fluids are expressed as a function of apparent kinematic viscosity, resulting in a modification of its classic definition. A few available definitions of such modified Reynolds numbers are given below.

The definition proposed by Collins and Schowalter (1963):

$$Re_{CS} = \frac{\rho V_i^{2-n} D^n}{K} \quad (6)$$

The definition proposed by Metzner and Reed (1955):

$$Re_{MR} = \frac{\rho V_i^{2-n} D^n}{K} 8 \left(\frac{n}{6n+2}\right)^n \quad (7)$$

The definition proposed by Marn and Ternik (2003):

$$Re_{MT} = \frac{\rho V_i D}{A(8V_i/D) + B} \quad (8)$$

The definition proposed by Poole and Ridley (2007):

$$Re_{Wall} = \frac{\rho V_i^{2-n} D^n}{K} \left(\frac{n}{2+6n}\right)^{n-1} \quad (9)$$

The definition proposed by Rudman et al. (2004):

$$Re_{Wall} = \frac{\rho V_i D}{\mu_w}; \mu_w = K^{1/n} \frac{\tau_w}{(\tau_w - \tau_y)^{1/n}} \quad (10)$$

For quantifying the Reynolds number in the subsequent analysis, we adopt the definition proposed by Metzner and Reed (1955), Eq. (7), which is switched to the classic expression of the Reynolds number only in the limit of $n = 1$. Note that the consistency index K can be interpreted as the dynamic viscosity only for $n = 1$. For any n other than 1, K does not have the dimension of dynamic viscosity. In this connection, we introduce a new parameter Re_N, identical to the classic Reynolds number at $n=1$. The definition of Re_N is as follows:

$$Re_N = \frac{\rho V_i D}{K} \quad (11)$$

where V_i is the area-averaged normal velocity at the inlet plane. We perform CFD simulations for incompressible fluid flow for a fixed geometry and mass inflow rate. Hence, V_i is constant (5 m/s) in all simulations. Moreover, Re_N does not vary since the consistency index (K) is independent of n and fixed to a particular value (0.001) in our simulations. The rationale behind this approach is to reveal the distinct role of n in the overall flow morphology while preserving the major dimensional input parameters. Thus, for a fixed Re_N, which is generally a dimensional parameter, we generate the solution dataset for various combinations of Re_{MR} and n. For a particular n, the
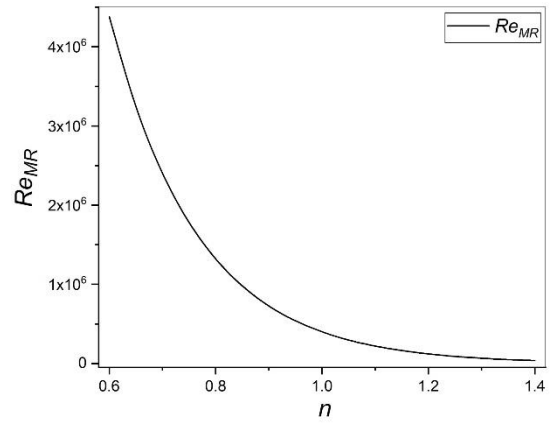
Fig. 1 Re_{MR} versus n for a fixed Re_N[Results presented in § 3 correspond to a fixed Re_N (4×10^5), while n is varied from 0.6 to 1.4.]

corresponding value of Re_{MR} can be predicted from the graph shown in Fig. 1.

The other way of performing the comparative study is to fix Re_{MR} for all n, adjusting the value of V_i with a change in n. This approach gives rise to a negligible variation of friction factor with a change in n. Since geometry is fixed for all simulations, the non-dimensional pressure difference (between the inlet and outlet of the pipe manifold) would remain insensitive with a change in n. Thus, it would be challenging to quantify the non-dimensional velocity and pressure changes along the bend with a change in n, adopting this approach. We follow the first approach for practical interest.

In the subsequent sections, we predict the non-Newtonian flow features within the bend and at far downstream by computational fluid dynamic (CFD) simulations. We focus only on the turbulent flow regime due to its versatile application. The bend's pressure losses and secondary flow characteristics of power-law fluids are examined in contrast with Newtonian fluids.

2. NUMERICAL MODELLING

2.1 Computational Domain

When a symmetrical velocity profile approaches a bend, it becomes asymmetric owing to secondary flow. This asymmetry manifests itself not only in terms of the stream-wise velocity profile but also in the formation of two uneven counter-rotating vortices (Fiedler 1997). Consequently, flow through a curved duct cannot be examined in an axisymmetric 2-dimensional flow domain. We consider a circular duct with an in-plane double bend (Fig. 1). The diameter (D) of the duct is 0.08 m, and the bend's curvature ratio $\bar{R}_c (\equiv R_c/R)$ is 9. Inlet and outlet planes are perpendicular to the Y-axis.

The direction of gravity is assumed along the negative Z-axis. Figure 2 shows two straight segments upstream and downstream of the bend. The upstream length (L_s) is 5D. The downstream length (L_d) is adjusted to realize a fully developed velocity profile before the outlet plane. A fully developed turbulent velocity profile is also assumed at the inlet.
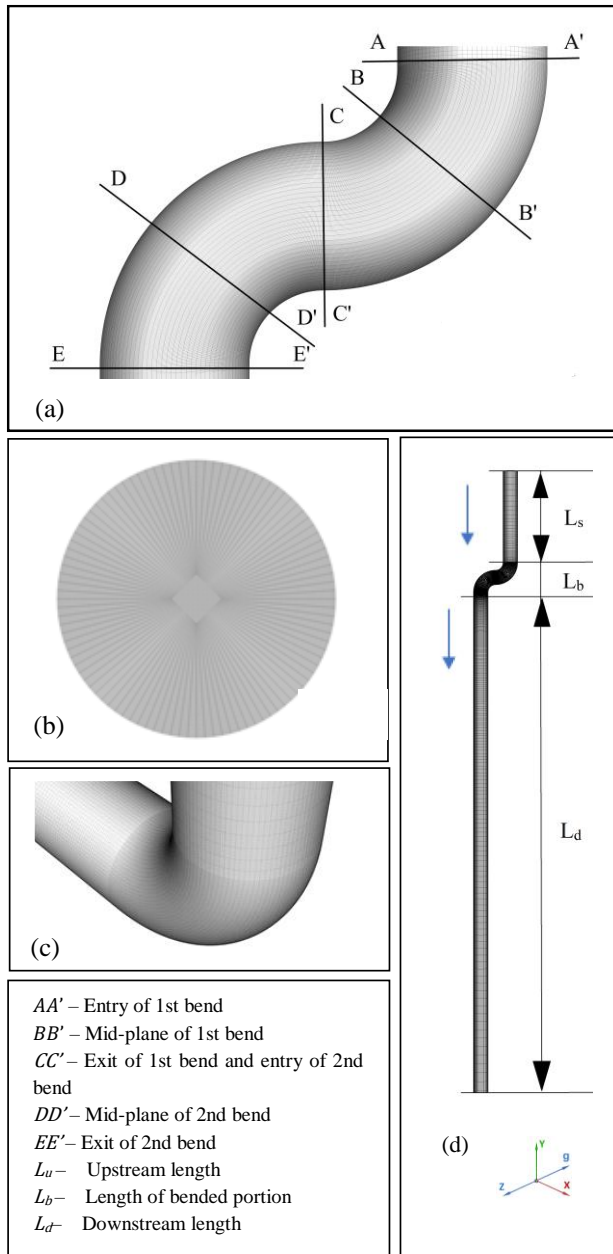
Fig. 2 Representation of the computational grid of the pipe manifold: (a) the full double-bend; (b) the inlet section; (c) the first bend's isometric view; (d) the full pipe manifold

2.2 Governing Equations

The steady-state Reynolds-averaged Navier–Stokes equations for incompressible flow are as follows:

$$\rho\vec{V}.\nabla\vec{V} + \nabla p - \mu.\nabla\vec{V} - \rho\nabla.\boldsymbol{R} = f \tag{12}$$

$$\nabla.\vec{V} = 0 \tag{13}$$

where, $\vec{V}$ is the velocity vector and $\boldsymbol{R}$ is the Reynolds Stress Tensor. According to the $k-\varepsilon$ turbulent model (Biswas & Eswaran, 2002),

$$\boldsymbol{R} = -\frac{2}{3}k\boldsymbol{I} + v_T(\nabla\vec{V} + \nabla\vec{V}^T). \tag{14}$$

$v_T(\equiv C_\mu\frac{k^2}{\varepsilon})$ designates kinematic eddy viscosity. k is the turbulent kinetic energy and ε is the dissipation of k. The equations for k and ε are as follows:

$$\vec{V}.\nabla k - \nabla.(D_k\nabla k) + \gamma_k k = F_k \tag{15}$$

$$\vec{V}.\nabla\varepsilon - \nabla.(D_\varepsilon\nabla\varepsilon) + \gamma_\epsilon\varepsilon = F_\epsilon \tag{16}$$

Here, $D_k(\equiv v_T/\sigma_k + v)$ and $D_\epsilon(\equiv v_T/\sigma_\varepsilon + v)$ are the diffusion coefficients; $\gamma_k(\equiv \varepsilon/k)$ and $\gamma_\epsilon(\equiv c_2\varepsilon/k)$ are the reaction coefficients; the source terms are $F_k\left(\equiv \frac{v_T}{2}\left|\nabla\vec{V} + \nabla\vec{V}^T\right|^2\right)$ and $F_\epsilon(\equiv \frac{c_1 k}{2}\left|\nabla\vec{V} + \nabla\vec{V}^T\right|^2)$. C_μ, σ_k, σ_ε, c_1 and c_2 are model constants (Launder & Spalding, 1974).

The working fluid is modelled by Ostwald-de Waele power-law relation, widely accepted for its simplicity and versatility. The constitutive relation for power-law fluids is already provided in Eq. (5). The apparent viscosity of non-Newtonian fluids is approximated by μ_{app} as follows:

$$\mu_{app} = K(\dot{\gamma}^{n-1}) \tag{17}$$

Other than consistency index and power law index, we also impose the maximum and minimum viscosity limits in our simulations. We set the maximum and minimum limits as $10^4 \times \mu_{n=1}$ and $10^{-4} \times \mu_{n=1}$, respectively (Yigit et al., 2016). $\mu_{n=1}$ designates the Newtonian base viscosity.

2.3 CFD Procedure

A fully structured three-dimensional hexahedron mesh (Fig. 2) has been used, composed of two regions, viz. core region (2-D mesh is square-shaped) and the region away from the core (2-D mesh constructed by radial and tangential grid lines). The boundary conditions used for the present simulations are as follows. At the inlet, $V_x = V_z = 0$ and $\bar{V}_y = V_i$, where the over-bar designates area-averaged quantities. V_i is used as the characteristic velocity scale for normalization. Fully-developed turbulent-flow velocity profiles for Newtonian and power-law fluids are generated in straight pipes and used as input velocity profiles in the inlet of the present computational domain. The value of turbulent intensity I specified at the inlet is according to the well-known experimental correlation, $I = 0.16 \times Re^{-0.125}$ (ANSYS, 2022).

At the outlet, a zero-gauge pressure is set. The pipe wall is assumed to be smooth and modelled by no slip and no penetration conditions. Simulations were performed by commercially available CFD software ANSYS FLUENT (ANSYS, 2022). Figure 2 displays a representative mesh used in the simulations. Here, we have used an optimum number of cells (9987500 cells) calibrated by a grid-independence test.

The CFD results for Newtonian fluids are validated with the experimental results of Laribi et al. 2003. A fully developed non-dimensional velocity profile at 91D downstream length at $Re = 1.9 \times 10^5$ is constructed from the experimental data of Laribi et al. 2003 and compared with present CFD results. The simulated result is also validated with the empirical $\frac{1}{7th}$ power-law profile, often used to capture turbulent mean flow behavior (Chant 2005). Our CFD results are in good agreement with both the experimental and empirical equations. The comparison is displayed in Table 1.

Table 1 Comparison of the numerical results with experimental results of Laribi et al. (2003) and 1/7th power law turbulent velocity profile [$n = 1, \overline{R}_c = 2, \frac{x}{D} = 91$]

x/D	V/V_{max}			Error (%)
	1/7th Law	Experiment	Simulation	
0.05	0.76	0.72	0.752	4.444
0.1	0.81	0.79	0.86	8.861
0.15	0.86	0.83	0.923	9.880
0.2	0.89	0.87	0.941	8.161
0.25	0.93	0.9	0.972	8.000
0.3	0.95	0.92	0.99	7.609
0.35	0.97	0.94	0.995	5.851
0.4	0.99	0.97	0.996	2.680
0.45	0.99	0.98	0.997	1.735
0.5	1	1	1	0.000
0.55	0.99	0.98	0.99	1.020
0.6	0.98	0.97	0.98	1.031
0.65	0.96	0.95	0.974	2.526
0.7	0.94	0.93	0.955	2.688
0.75	0.91	0.9	0.938	4.222
0.8	0.88	0.87	0.914	5.057
0.85	0.84	0.83	0.885	6.627
0.9	0.78	0.79	0.834	5.570
0.96	0.72	0.72	0.728	1.111
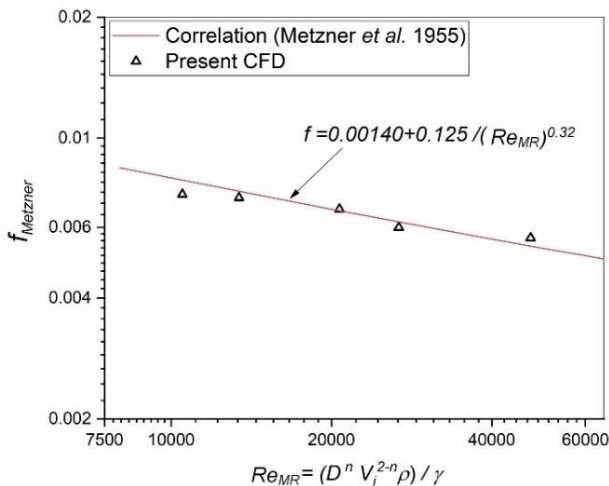
Fig. 3 Validating the friction factor of non-Newtonian fluid flow: present computation versus the experimental correlation given in Metzner and Reed 1955

To validate the results for power law fluids, the benchmark correlation proposed by Metzner and Reed. (1955) is used here. Figure 3 shows that the results obtained in the CFD simulations are in good agreement with the experimental correlation.

3. RESULTS & DISCUSSION

A bend in a duct affects the primary or stream-wise flow through the duct, giving rise to a cross-stream secondary flow perpendicular to the primary flow. Fluid flow at the inner radius of the bend is subtly different from its outer radius. The flow inside the double-bend geometry also evolves spatially. We analyze the flow characteristics at various locations within the double-bend. For this purpose, we have selected five representative sections: entry of the first bend (AA'), mid-plane of the first bend (BB'), junction of two bends (CC'), mid-plane of the second bend (DD') and exit of the second bend (EE'). A study capturing the evolution of secondary flow downstream of the second bend is also fascinating. We discuss the pertinent details obtained from our CFD simulations.

3.1 Transition of Velocity Profiles inside Bend

We study the effect of bend geometry on the velocity magnitude normalizing it by V_i. The radial variation of the normalized velocity magnitude is determined at different sections within the bend, which is shown in Fig. 4. Radial velocity distributions are captured at three different n viz. 0.6, 1 and 1.4 for comparison. A similar spatial evolution is observed for all values of n. It has been clearly observed that at the entrance of the first bend, the velocity profile is symmetrical, and the maximum velocity is found at the mid-portion ($r/D=0$, where r is defined as the local radius such that r/D is varied from -0.5 to 0.5 at two extreme ends). However, when the flow enters the bend the maximum velocity region moves towards the outer core of the bend. For the first bend, the outer core lies from $r/D=0$ to $r/D=0.5$. Thus, a gradual shifting of the peak velocity towards $r/D=0.5$ is observed up to the exit of the first bend. For the second bend, the bend curvature's direction is reversed; and, the outer core lies from $r/D=0$ to $r/D=-0.5$. Hence, the maxima shift towards $r/D=-0.5$. Previous researchers (Rohrig et al., 2015; Dutta et al., 2016) have already reported the radial shifting for Newtonian fluid flow within a single bend. We illustrate the radial shifting in double-bend geometry, extending the study to a non-Newtonian flow regime.

A non-uniform distribution of momentum influenced by the centrifugal force causes such a shift of maxima. The faster-moving fluid particles are pushed towards the outer core. With a spatial change in the bend-wall's direction-normal, the outer core also changes its position. Accordingly, the maxima appear in various locations. Thus, the bend in the duct geometry attributes to a redistribution of momentum within the duct in a passive mean. As a result, the duct flow exhibits an accelerating-decelerating feature, for which fluid particles accelerate along the outer wall and decelerate along the inner wall. A small value of $\overline{R}_c$ is more favorable for accelerating-decelerating flow. The camel's-back-shaped velocity profiles shown in Fig. 4 near the junction of the two bends are attributed to this accelerating-decelerating flow (Dutta & Nandi, 2015).

(a)

(b)

(c)
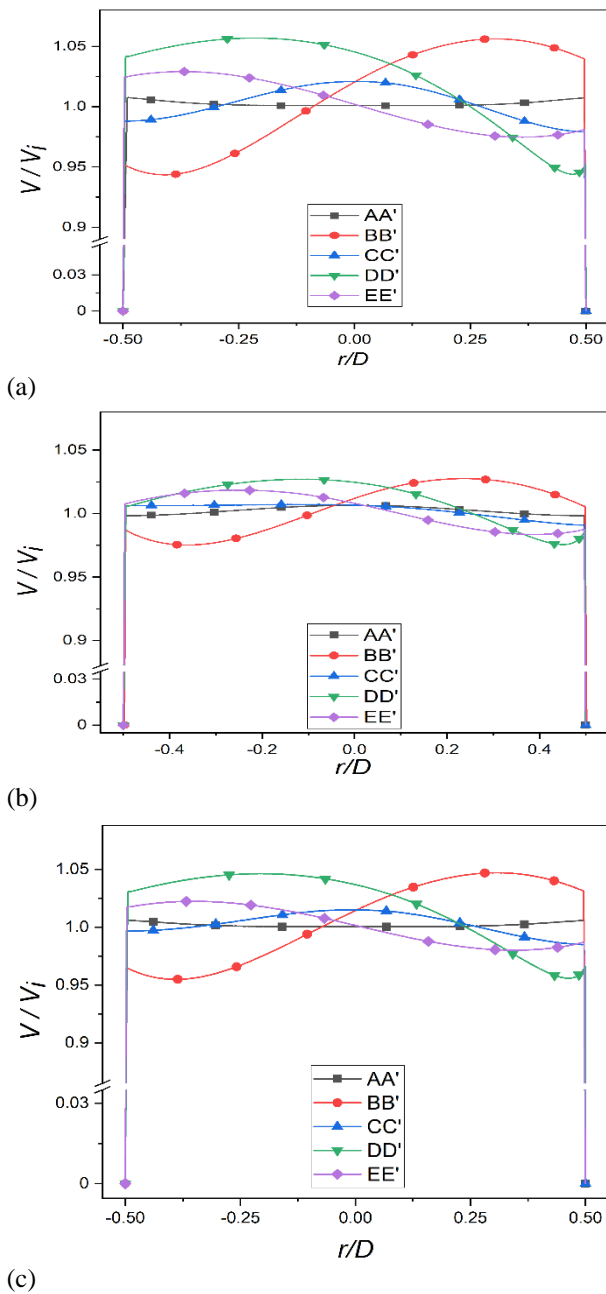
Fig. 4. Normalized velocity Distribution within the double bend for (a) *n*=0.6, (b) *n*=1.0, (c) *n*=1.4.

## 3.2 Reestablishment of Primary Velocity & Decay of Secondary Velocity After Bend

The fluid particles boosted by the centrifugal force develop an in-plane velocity component inside the duct. While the primary velocity component (V_p) is due to the mainstream through-flow, the in-plane velocity component gives rise to a secondary flow perpendicular to the mainstream. We designate the secondary velocity component by V_s, defined as the magnitude of in-plane velocity components. This section examines the developments of V_p and V_s downstream of the bend. For illustrations, we normalize both components by the inlet velocity V_i. Figure 5 shows how the normalized secondary velocity (V_s/V_i) decays along the non-dimensional downstream length, L_d/D. In the course of this study, it is

found that a small inlet Reynolds number and a large curvature ratio values expedite the decay of secondary velocity. Further, the strength of secondary flow at the bend exit increases with decreasing *n*, as illustrated in Fig. 5. However, it is surprising to note that the downstream length required to eliminate the secondary flow exhibits insensitivity with changes in *n*. Similar insensitivity was also observed in the case of laminar pipe flow of power-law fluids; see Poole and Ridley (2007) for details.
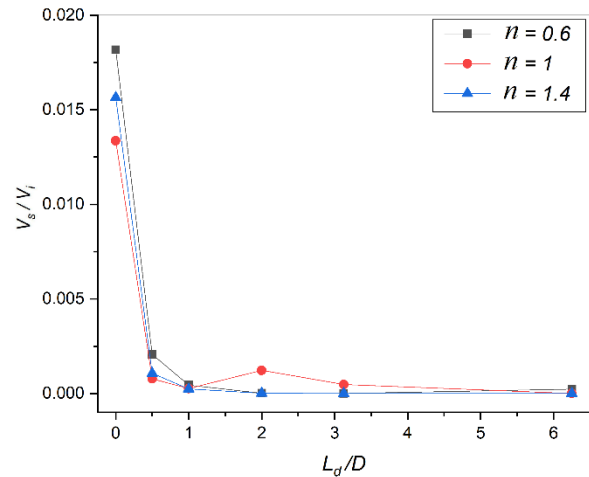
Fig. 5 Decay of Secondary velocity in the straight pipe downstream of the double bend

When the flow exits the bend portion and enters the downstream straight pipe, the primary flow gradually re-establishes its fully-developed state. The re-establishment of fully-developed primary velocity and decay of secondary velocity is not a separate phenomenon; instead, they occur simultaneously. It would be interesting to monitor the spatial evolution of the primary velocity on transverse cutting planes normal to the *y*-axis. For this purpose, we select two representative cutting planes at L_d/D=0 and L_d/D=1, respectively. Figure 6 displays the contours of normalized primary velocity on these two cutting planes. It is observed that the non-axisymmetric distribution gets converted to a nearly axisymmetric distribution in the process of such spatial evolution. Further, the non-axisymmetric contours are observed far downstream in the near-wall region while entirely eliminated in the core region. The difference between the behavior of the core and near-wall regions is more prominent for non-Newtonian fluids rather than Newtonian fluids. The phenomenon is attributed to the near wall shear stress affecting the power-law viscosity, so the disturbance after the bend is carried forward far downstream. Figure 7 shows the secondary velocity contours just after the bend and at L_d/D=1. The secondary motion is more pronounced for shear-thinning fluids than shear-thickening and Newtonian fluids. This observation corroborates the average trend of V_s displayed previously in Fig. 5. The decay of secondary flow within a short downstream length is clearly reflected in the contour values for all representative cases. Figure 7 also shows that the magnitude of V_s at the bend downstream attains a peak value near the top and bottom ends of the horizontal duct.
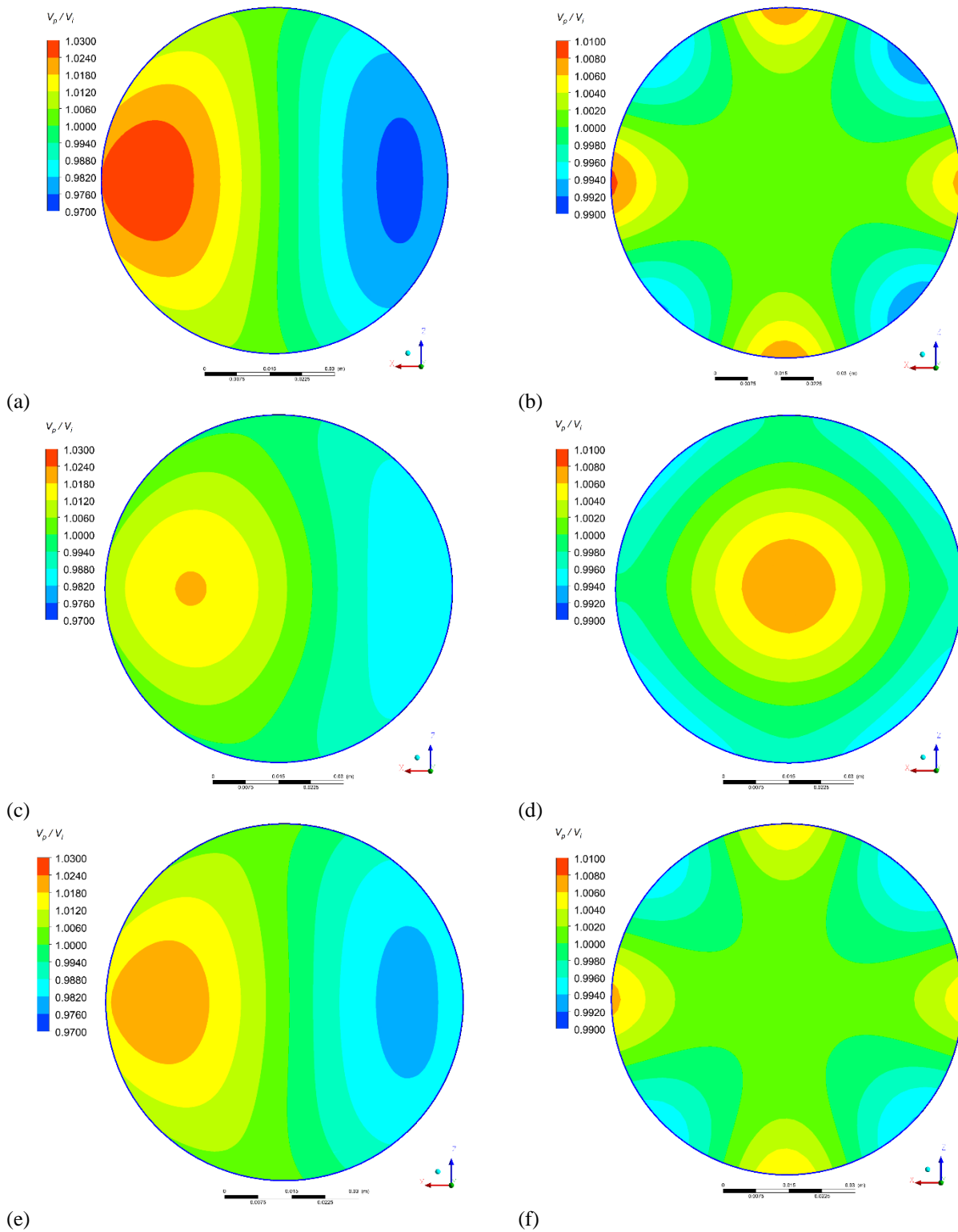
Fig. 6 Contours of the normalized primary velocity in the straight pipe downstream of the double bend [for (a) $L_d/D=0$, $n=0.6$ (b) $L_d/D=1$, $n=0.6$ (c) $L_d/D=0$, $n=1$ (d)$L_d/D=1$, $n=1$ (e) $L_d/D=0$, $n=1.4$ (f) $L_d/D=1$, $n=1.4$]

3.3 Velocity Enhancement and Pressure Drop Characteristics

Fluid flow in the bend portion of a duct experiences a greater pressure loss than in the straight portion, which is valid for Newtonian and power-law fluids (Alexander 1905; Ito, 1960; Żelasko & Niezgoda-Żelasko, 2010; Debnath et al., 2017). This additional pressure loss is associated with a corresponding increase in velocity. We invoke a new non-dimensional parameter, viz.

enhancement ratio (ϵ), to quantify the velocity rise. The enhancement ratio is defined as follows:

$$\epsilon = \frac{\text{average velocity magnitude at the exit of bend}}{\text{average velocity magnitude at the entry}} \quad (18)$$

Since a double bend geometry is considered here, ϵ can be determined separately for the first and second bends. Figure 2 shows that the first bend is extended from plane AA' to plane CC', and the second bend is extended from plane CC' to plane EE'. Accordingly, the

(a)

(b)

(c)

(d)

(e)

(f)
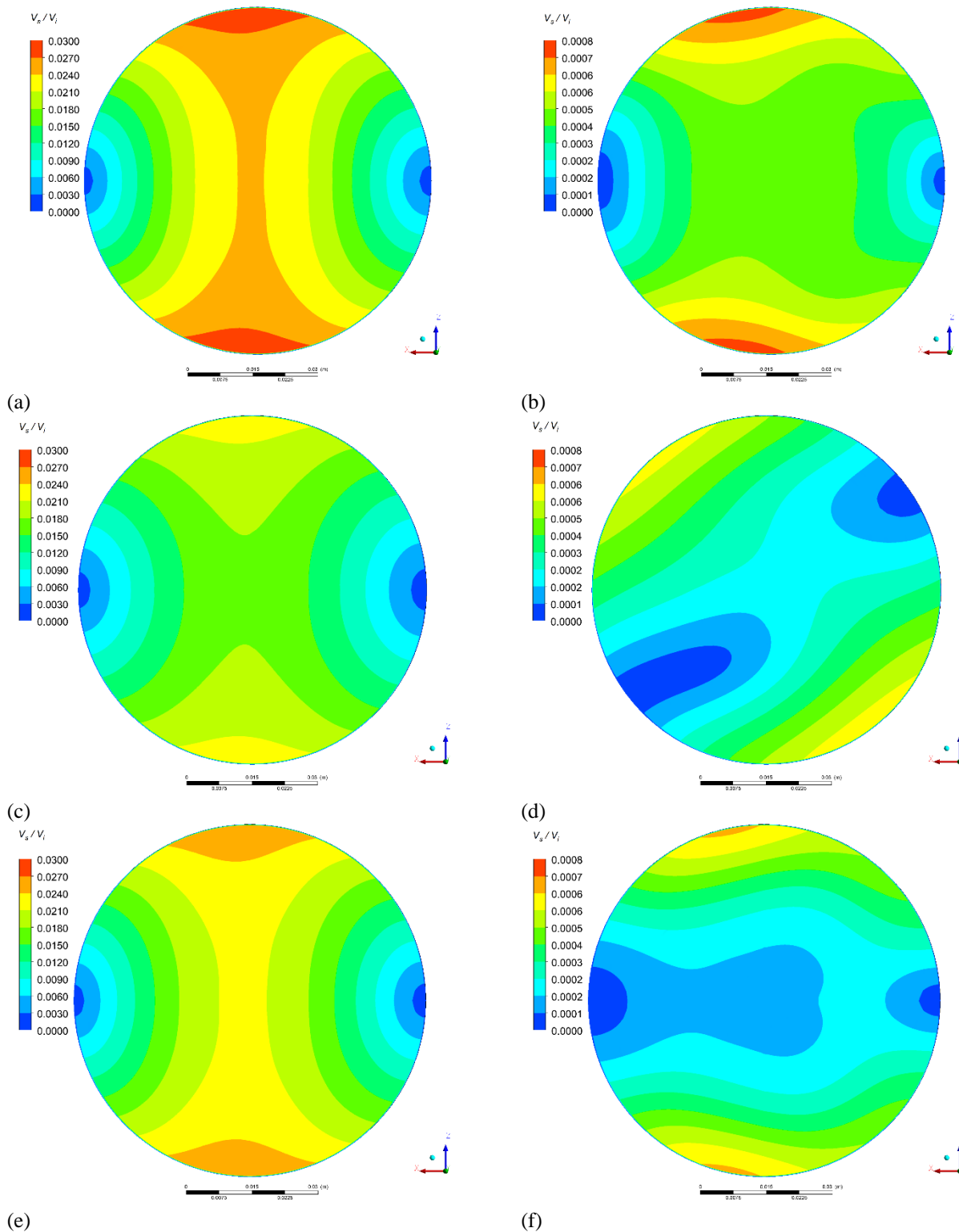
Fig. 7 Contours of the normalized secondary velocity in the straight pipe downstream of the double bend [for (a) $L_d/D=0$, $n=0.6$ (b) $L_d/D=1$, $n=0.6$ (c) $L_d/D=0$, $n=1$ (d)$L_d/D=1$, $n=1$ (e) $L_d/D=0$, $n=1.4$ (f) $L_d/D=1$, $n=1.4$]

enhancement ratio for the first and second bends are denoted by the symbols ϵ_{AC} and ϵ_{CE}, respectively. The values of ϵ_{AC} and ϵ_{CE} are shown in Fig. 8a. For $n \geq 1$, the velocity enhancement occurs mainly in the first bend. On the other hand, both bends contribute equally in the case of shear-thinning fluids. Therefore, considering the bend combination, the overall enhancement ratio (ϵ) is more significant for shear-thinning fluids. For the representative

case, the values of ϵ are obtained as 1.0026, 1.0019 and 1.0003 for $n = 0.6, 1$ and 1.4, respectively.

Similar to the case of velocity enhancement, we predict the pressure drop separately due to the first and second bends. We introduce a parameter, viz., non-dimensional pressure difference (φ), to gauge the pressure loss across the bend. For the first and second bends, φ is defined as follows:
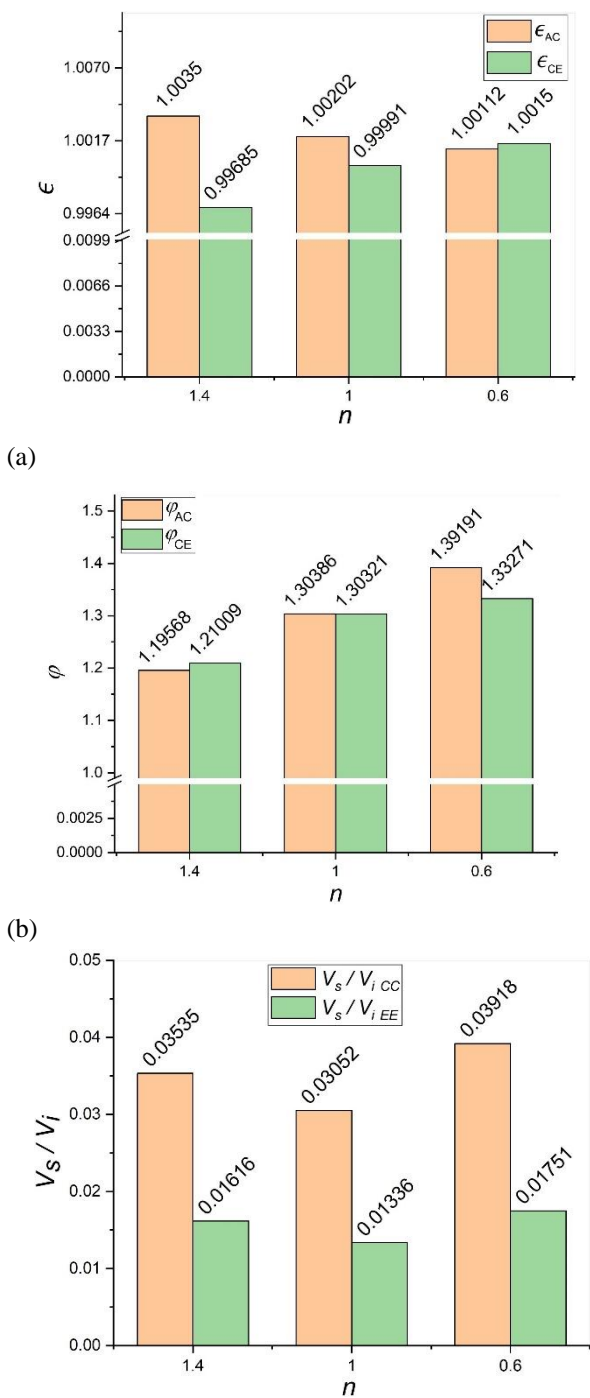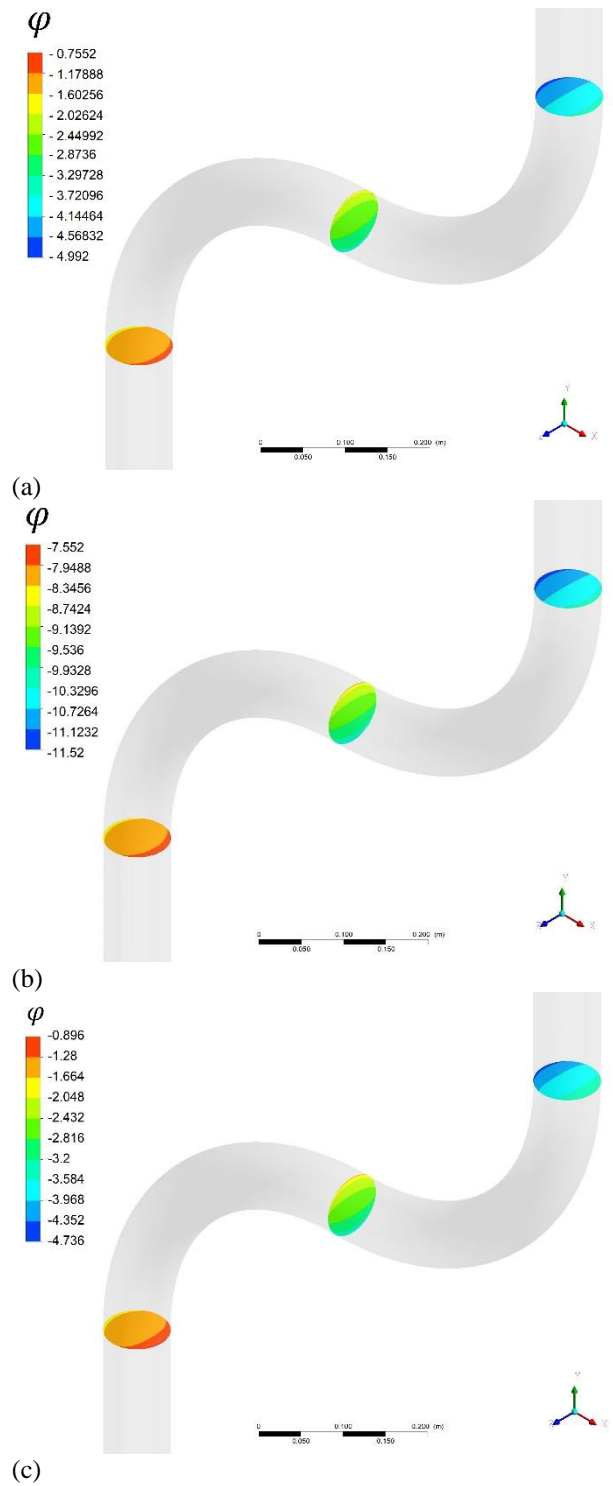
(a)

(b)

(c)

Fig. 8 Variation of a few important parameters along the bend (a) Enhancement ratio, (b) Non-dimensional pressure difference and (c) Normalized secondary velocity

(a)

(b)

(c)

Fig. 9 Distribution of pressure at different sections (AA', CC' and EE') along the bend inside bend (a) n=0.6, (b) n=1.0, (c) n=1.4

$$\varphi_{AC} = (P_{AA'} - P_{CC'})/\frac{1}{2}\rho V_i^2 \qquad (19)$$

$$\varphi_{CE} = (P_{CC'} - P_{EE'})/\frac{1}{2}\rho V_i^2 \qquad (20)$$

Figure 8b displays that both φ_{AC} and φ_{CE} increase with a decrease of n. From Fig. 8a and 8b, we conclude that the higher the values of φ higher will be the ϵ. Actually, the velocity enhancement occurs due to the conversion of the pressure head to kinetic energy. Finally, we determine V_s/V_i at the end of the first and second bends (i.e. on CC' and EE'), respectively. Here, V_s/V_i is

indicative of the secondary kinetic energy evolved due to the presence of the bends. We compare the values of V_s/V_i due to the two bends, as depicted in Fig. 8c. It is observed that the first bend promotes the strength of the secondary flow, whereas the second bend reduces the strength, reversing the flow's direction. The secondary flow strength is found to be more in power-law fluids than in Newtonian fluids, which is in line with the observations given by Yoon et al. (2017).
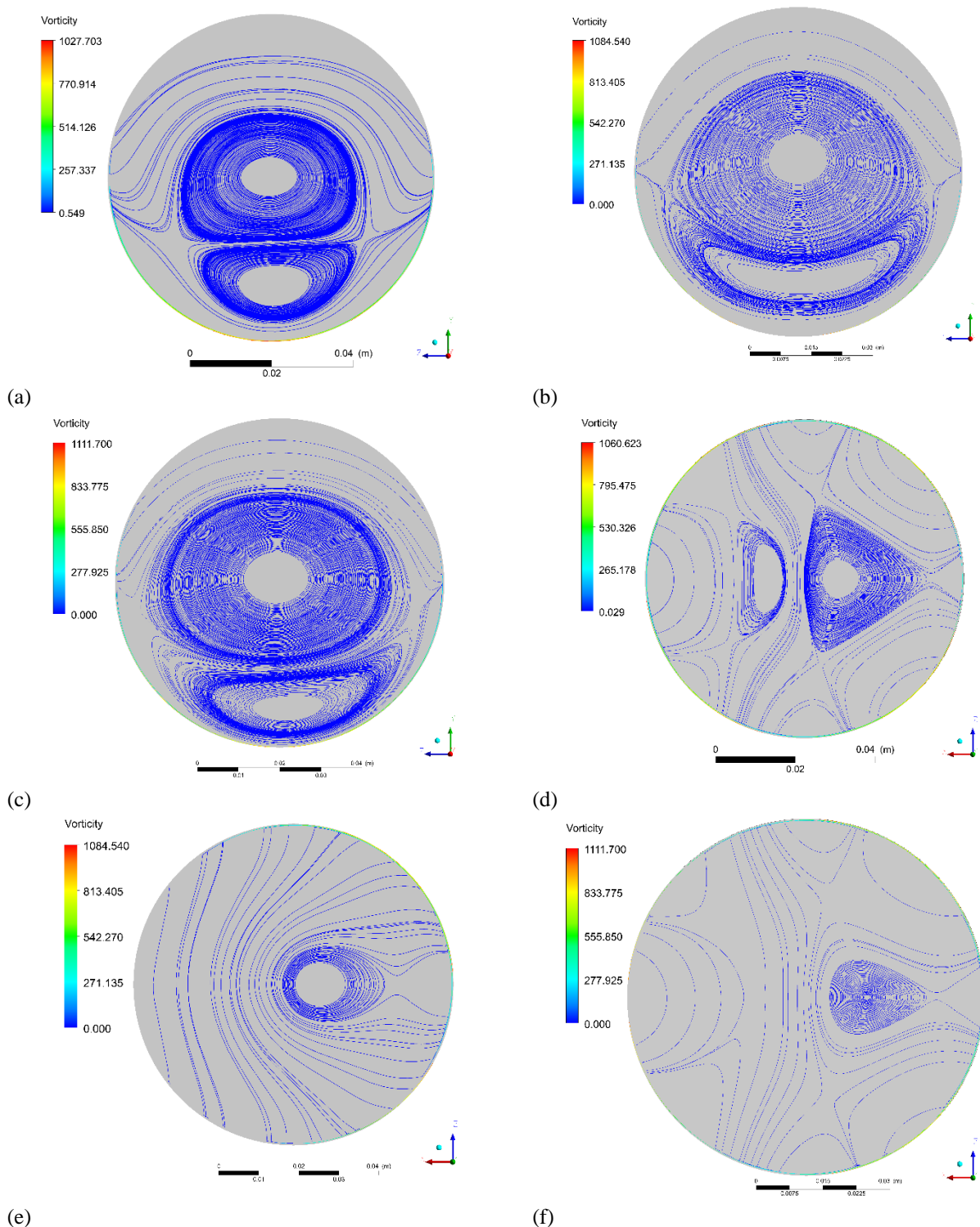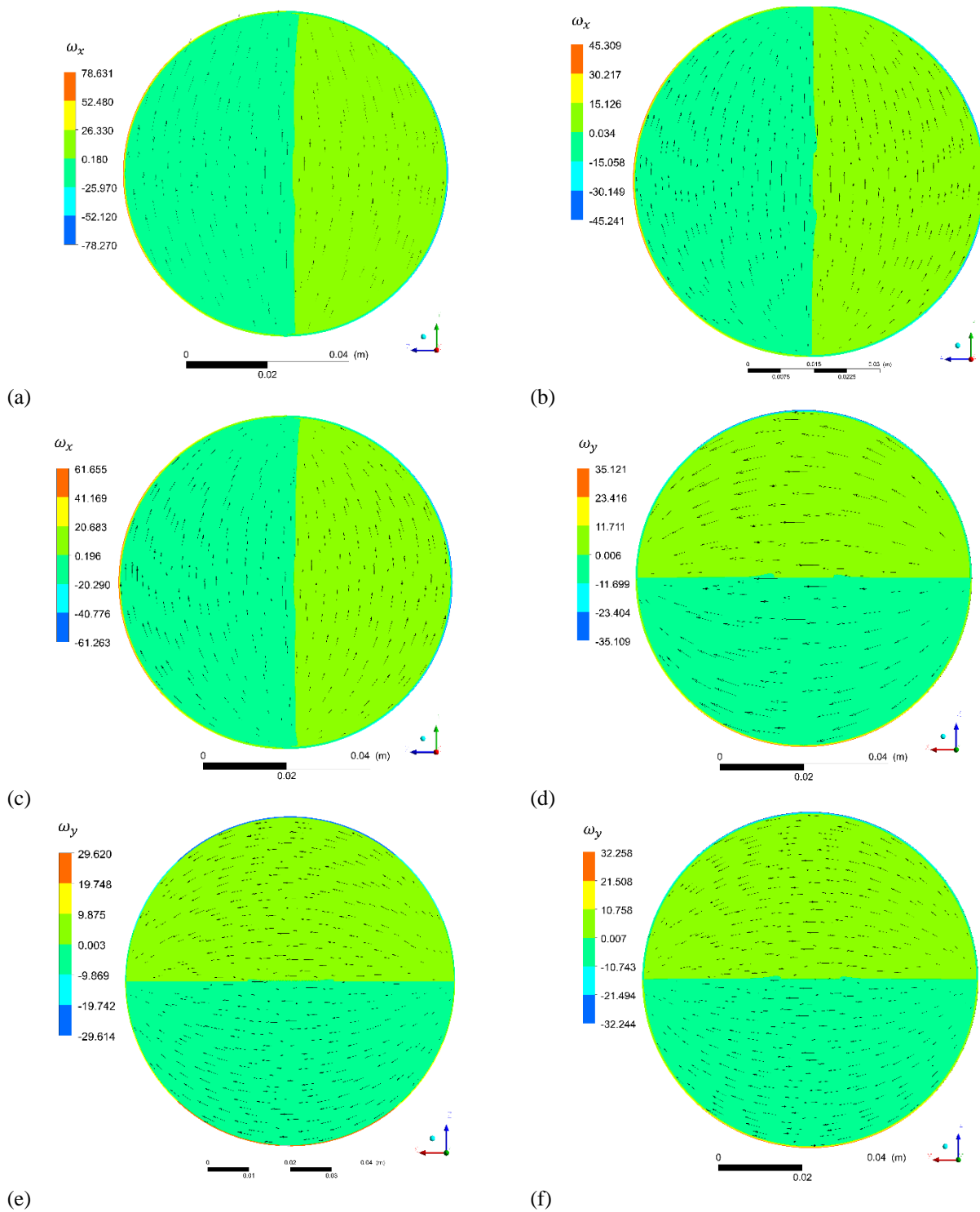
Fig. 10. Vorticity streamlines at the exit of the first bend (CC') for (a) *n*=0.6, (b) *n*=1.0, (c) *n*=1.4; Vorticity streamlines at the exit of the second bend (EE') for (d) *n*=0.6, (e) *n*=1.0, (f) *n*=1.4

3.4 Pressure Variation Inside Bend

Non-dimensional pressure $(P/\frac{1}{2}\rho V_i^2)$ contours are captured at three distinct sections, AA', CC' and EE', for $n = 0.6, 1$ and 1.4 (Fig. 9). The planes AA', EE' and CC' are located at the first bend's entrance, the second bend's exit and their junction, respectively. A radial pressure gradient, either inward or outward, is observed on the three planes. In section AA', the pressure rises towards the inner core. The bend's curvature reverses beyond CC',

where the second bend starts. Accordingly, CC' is the junction of the first bend's outer core and the second bend's inner core. At CC', the high-pressure zone is shifted towards the inner core of the second bend. Again, at section EE', the pressure rises towards the outer core of the second bend. This shift is attributed to a change in bend curvature at the exit of the second bend. Newtonian and non-Newtonian fluids exhibit similar qualitative trends, as depicted in Fig. 9. The contour values demonstrate

Fig. 11 Vorticity contours at the exit of the first bend (CC') for (a) *n=0.6*, (b) *n=1.0*, (c) *n=1.4*, Vorticity contours at the exit of the second bend (EE') for (d) *n=0.6*, (e) *n=1.0*, (f) *n=1.4*

a continuous pressure drop along the length of the duct's bend.

3.5 Vorticity Streamlines

The vorticity function is utilized to characterize the spinning motion of the continuum (fluid domain). Mathematically, vorticity, $\omega = \vec{\nabla} \times \vec{v}$, where, $\vec{\nabla}$ is the nabla operator, and $\vec{v}$ is the velocity vector at a point. We determine the in-plane vorticity streamlines using the vorticity components. Fig. 10 displays vorticity streamlines on planes CC' and EE' for $n = 0.6, 1, 1.4$. The opposite sign of vorticity indicates the presence of a pair of counter- rotating cells (Fig. 10 and 11). Since plane CC' is perpendicular to *X*-axis and EE' is perpendicular to *Y*-axis (Fig. 2), the orientation of the negative and positive vorticity regions are subtly altered, as depicted in Fig. 11. Accordingly, the pattern of vorticity-streamlines changes, and the vertically aligned cells change their orientation to become horizontally aligned (Fig. 10). The reversal of bend curvature is responsible for a conversion of *X*-vorticity to *Y*-vorticity, which affects the strength of

2434

vortices. The counter-rotating vortices lose their strength while changing their orientation within the second bend. The drop of vorticity magnitude from CC' to EE' is more for Newtonian fluids.

4. CONCLUSION

This study investigates the characteristics of Newtonian and non-Newtonian fluid flow (shear thinning and shear thickening) through a pipe manifold which contains a double bend. The Ostwald–de Waele's power law model is adopted to predict the rheological behavior of the working fluids. The $k - \varepsilon$ turbulence model is suitably used to solve the RANS equations for resolving the flow physics. The CFD results match well with the previous experimental data. The major observations lead to the following conclusions:

- The symmetrical velocity profiles at the bend inlet become skewed towards the outer core of the curved pipe due to a non-uniform distribution of momentum caused by the centrifugal effect.

- Internal flow through skewed pipe gives rise to Prandtl's secondary flow of the first kind. A fully developed flow is disturbed when it enters bend or bend combinations. The flow regains its fully developed characteristic gradually after the bend. Consequently, the secondary flow progressively vanishes. This decay of secondary flow accelerates when the curvature ratio is large, and the Reynolds number is small.

- The strength of the secondary flow at the bend's exit depends on the flow behavior index (n). It is higher for lower values of n.

- The stream-wise velocity component exhibits a non-axisymmetric distribution at the bend's exit, which attains axisymmetry within a short downstream length due to turbulent mixing. The exception is the non-Newtonian near-wall region which retains non-axisymmetry due to spatially non-uniform wall stress governed by the constitutive behavior.

- Some additional pressure loss due to bend is captured, associated with a simultaneous rise in area-weighted average velocity. We successfully quantify the velocity gain due to the bend by a newly defined dimensionless number, viz. enhancement ratio (ϵ). The value of ϵ is found to be the maximum for shear-thinning fluid flow and the minimum for shear-thickening fluid flow. Similarly, the amount of pressure drop rises with a decrease in n.

- A radial pressure gradient acts inside the double bend, which directs inward or outward depending on the curvature. The radial pressure gradient is the motive force for the secondary flow.

- Two counter-rotating vortices are captured inside the first bend portion of the double bend geometry, losing their strength in the second bend. A more significant drop of vorticity magnitude within the second bend portion is observed when n tends to 1.

CONFLICTS OF INTEREST

The authors whose names are listed immediately below certify that they have NO affiliations with or involvement in any organization or entity with any financial interest (such as honoraria; educational grants; participation in speakers' bureaus; membership, employment, consultancies, stock ownership, or other equity interest; and expert testimony or patent-licensing arrangements), or non-financial interest (such as personal or professional relationships, affiliations, knowledge or beliefs) in the subject matter or materials discussed in this manuscript.

AUTHORS CONTRIBUTION

A. Banerjee: Data curation (equal); Formal analysis (equal); Investigation (equal); Software (equal); Validation (equal); Writing – original draft (equal); Writing – review & editing (equal). S. Sengupta: Conceptualization (equal); Data curation (equal); Formal analysis (equal); Methodology (equal); Resources (equal); Supervision (equal); Writing – original draft (equal); Writing – review & editing (equal). S. Pramanik: Supervision (equal).

REFERENCES

Aichouni, M., Kolsi, L., Ait-Messaoudenne, N., & Aich, W. (2016). Computational study of the performance of the Etoile flow conditioner. *International Journal of Advanced and Applied Sciences*, 3, 25-30. http://dx.doi.org/10.21833/ijaas.2016.09.005

Alexander, C. W. L. (1905). The resistance offered to the flow of water in pipes by bends and elbows. *Minutes of the Proceedings of the Institution of Civil Engineers*, 159, 341–364 . https://doi.org/10.1680/imotp.1905.16457

ANSYS, Inc. (2022). *ANSYS Fluent User's Guide*. Release R1, Canonsburg, U.S.A.

Barua, S. N. (1963). On secondary flow in stationary curved pipes. *The Quarterly Journal of Mechanics and Applied Mathematics*, 16(1), 61-77. https://doi.org/10.1093/qjmam/16.1.61

Berger, S. A., Talbot, A. L., & Yao, L. S. (1983). Flow in curved pipes. *Annual Review of Fluid Mechanics*, 15, 461-512. https://doi.org/10.1146/annurev.fl.15.010183.002333

Bíbok, M., Csizmadia, P., & Till, S. (2020). Experimental and numerical investigation of the loss coefficient of a 90 pipe bend for power-law fluid. *Periodica Polytechnica-Chemical Engineering*, 64(4), 469-478. https://doi.org/10.3311/PPch.14346

Biswas, G., & Eswaran, V. (2002). *Turbulent flows: fundamentals, experiments and modeling. CRC Press*.

Bradshaw, P. (1987). Turbulent secondary flows. *Annual Review of Fluid Mechanics*, 19(1), 53–74. https://doi.org/10.1146/annurev.fl.19.010187.000413

Cabral, R. A. F., Telis, V. R. F., Park, K. J., & Telis-

Romero, J. (2011) Friction losses in valves and fittings for liquid food products. *Food and Bioproducts Processing*, 89(4), 375–382. https://doi.org/10.1016/j.fbp.2010.08.002

Canton, J., Schlatter, P., & Örlü, R. (2016). Modal instability of the flow in a toroidal pipe. *Journal of Fluid Mechanics*, 792, 894-909. https://doi.org/10.1017/jfm.2016.104

Chant, L. J. (2005). The venerable 1/7th power law turbulent velocity profile: a classical nonlinear boundary value problem solution and its relationship to stochastic processes. *Applied Mathematics and Computation*, 161(2), 463-474. https://doi.org/10.1016/j.amc.2003.12.109

Chu, Y. M., Jakeer, S., Reddy, S. R. R., Rupa, M. L., Trabelsi, Y., Khan, M. I., & Eldin, S. M. (2023). Double diffusion effect on the bio-convective magnetized flow of tangent hyperbolic liquid by a stretched nano-material with Arrhenius Catalysts. *Case Studies in Thermal Engineering*, 44, 102838. https://doi.org/10.1016/j.csite.2023.102838

Cieślicki, K., & Piechna, A. (2012). Can the dean number alone characterize flow similarity in differently bent tubes?. *Journal of fluids engineering*, 134(5). https://doi.org/10.1115/1.4006417

Collins, M., & Schowalter, W. R. (1963). Behavior of non-Newtonian fluids in the entry region of a pipe. *AIChE Journal*, 9(6), 804-809. https://doi.org/10.1002/aic.690090619

Csizmadia, P. (2016). Sűrűzagy keverőben lezajló áramlási folyamatok kísérleti és numerikus vizsgálata. [Doctoral dissertation, Budapest University of Technology and Economics (Hungary)].

Csizmadia, P., & Hős, C. (2013). LDV measurements of Newtonian and non-Newtonian open-surface swirling flow in a hydrodynamic mixer. *Periodica Polytechnica Mechanical Engineering*, 57(2), 29–35. https://doi.org/10.3311/PPme.7045

Dean, W. R. (1927). XVI. Note on the motion of fluid in a curved pipe. *The London, Edinburgh, and Dublin Philosophical Magazine and Journal of Science*, 4(20), 208-223. https://doi.org/10.1080/14786440708564324

Debnath, S., Bandyopadhyay, T. K., & Saha, A. K. (2017). CFD analysis of non-newtonian pseudo plastic liquid flow through bends. *Periodica Polytechnica Mechanical Engineering*, 61(3), 184-203. https://doi.org/10.3311/PPme.9494

Dey, D., & Mahanta, B. (2022). *Rheology of power-law nano-fluid flow past a stretching sheet*. Advances in Thermofluids and Renewable Energy: Select Proceedings of TFRE 2020. Springer Singapore. https://doi.org/10.1007/978-981-16-3497-0_6

Dutta, P., & Nandi, N. (2015). Effect of reynolds number and curvature ratio on single phase turbulent flow in pipe bends. *Mechanics and Mechanical Engineering*, 19(1), 5-16.

Dutta, P., Saha, S. K., Nandi, N., & Pal, N. (2016). Numerical study on flow separation in 90° pipe bend under high Reynolds number by k-ε modelling. *Engineering Science and Technology, an International Journal*, 19(2), 904-910. https://doi.org/10.1016/j.jestch.2015.12.005

Ellahi, R., Sait, S. M., Shehzad, N., & Mobin, N. (2019). Numerical simulation and mathematical modeling of electro-osmotic Couette–Poiseuille flow of MHD power-law nanofluid with entropy generation. *Symmetry*, 11(8), 1038. https://doi.org/10.3390/sym11081038

Esfe, M. H., & Rostamian, H. (2017). Non-Newtonian power-law behavior of TiO_2/SAE 50 nano-lubricant: an experimental report and new correlation. *Journal of Molecular Liquids*, 232, 219-225. https://doi.org/10.1016/j.molliq.2017.02.014

Fiedler, H. E. (1997). A note on secondary flow in bends and bend combinations. *Experiments in Fluids*, 23(3), 262-264. https://doi.org/10.1007/s003480050109

Ito, H. (1960). Pressure losses in smooth pipe bends. *Journal of Basic Engineering*, 82(1), 131–140. https://doi.org/10.1115/1.3662501

Ito, H. (1987). Flow in curved pipes. *JSME international Journal*, 30(262), 543-552. https://doi.org/10.1299/jsme1987.30.543

Kalpakli Vester, A., Örlü, R., & Alfredsson, P. H. (2016). Turbulent flows in curved pipes: recent advances in experiments and simulations. *AppliedMechanics Reviews*, 68(5). https://doi.org/10.1115/1.4034135

Khali, S., Nebbali, R., & Bouhadef, K. (2017). Effect of a porous layer on Newtonian and power-law fluids flows between rotating cylinders using lattice Boltzmann method. *Journal of the Brazilian Society of Mechanical Sciences and Engineering*, 39, 3881-3895. https://doi.org/10.1007/s40430-017-0809-6

Khali, S., Bousri, A., Hamadouche, A., Eddine Ameziani, D., Bennacer, R., &Nebbali, R. (2022). Double diffusive convection of power law fluids through taylor–couette flow. *Journal of Thermophysics and Heat Transfer*, 36(2),328-341. https://doi.org/10.2514/1.T6405

Khali, S., & Nebbali, R. (2023). Numerical study of the effect of a power-law fluid flow structures on levels of mixing in a taylor couette configuration. *Journal of Applied Fluid Mechanics*, 16(6), 1232-1242. https://doi.org/10.47176/JAFM.16.06.1683

Lai, Y., So, R. M. C., & Zhang, H. S. (1991). Turbulence-Driven secondary flows in a curved pipe, *Theoretical and Computational Fluid Dynamics*, 3(3), 163–180. https://doi.org/10.1007/BF00271800

Launder, B. E., & Spalding, D. B. (1983). *The numerical computation of turbulent flows*. Numerical Prediction of Flow, Heat Transfer, Turbulence and Combustion. Pergamon. https://doi.org/10.1016/B978-0-08-030937-8.50016-7

Lambride, C., Syrakos, A., & Georgiou, G. C. (2023). Entrance length estimates for flows of power-law fluids in pipes and channels. *Journal of Non-Newtonian Fluid Mechanics*, 317, 105056. https://doi.org/10.1016/j.jnnfm.2023.105056

Laribi, B., Amrane, A. A., & Youcefi, A. (2013). *Numerical analysis of the discharge coefficient with disturbers for flow metring accuracy.* 16th International Congress of Metrology. EDP Sciences. https://doi.org/10.1051/metrology/201302001

Laribi, B., Wauters, P., & Aichouni, M. (2003). Comparative study of aerodynamic behavior of three flow conditioners. *European Journal of Mechanical and Environmental Engineering*, 48(1), 21-30. https://aichouni.tripod.com/Papers/bsme2003_part1.pdf

Laribi, B., Wauters, P., & Youcefi, A. (2010, January). *Numerical investigation of contribution of three flow conditioners in the development and establishment of turbulent flows.* Fluids Engineering Division Summer Meeting (Vol. 49491, pp. 233-238). https://doi.org/10.1115/FEDSM-ICNMM2010-31291

Li, S., Raghunath, K., Alfaleh, A., Ali, F., Zaib, A., Khan, M. I., & Puneeth, V. (2023a). Effects of activation energy and chemical reaction on unsteady MHD dissipative Darcy–Forchheimer squeezed flow of Casson fluid over horizontal channel. *Scientific Reports*, 13(1), 2666. https://doi.org/10.1038/s41598-023-29702-w

Li, S., Ali, F., Zaib, A., Loganathan, K., Eldin, S. M., & Ijaz Khan, M. (2023b). Bioconvection effect in the Carreau nanofluid with Cattaneo–Christov heat flux using stagnation point flow in the entropy generation: Micromachines level study. *Open Physics*, 21(1), 20220228. https://doi.org/10.1515/phys-2022-0228

Marn, J., & Ternik, P. (2003). Use of quadratic model for modelling of fly ash-water mixture. *Applied Rheology*, 13(6), 286-296. https://doi.org/10.1515/arh-2003-0018

Mendes, P. R. S., & Dutra, E. S. (2004). A viscosity function for viscoplastic liquids. *Annual Transactions of the Nordic Rheology Society*, 12, 183-188.

Metzner, A. B., & Reed, J. C. (1955). Flow of non-Newtonian fluids—correlation of the laminar, transition, and turbulent-flow regions. *Aiche Journal*, 1(4), 434-440. https://doi.org/10.1002/aic.690010409

Mitsoulis, E. (2007). Annular extrudate swell of pseudoplastic and viscoplastic fluids. *Journal of Non-Newtonian Fluid Mechanics*, 141(2-3), 138-147. https://doi.org/10.1016/j.jnnfm.2006.10.004

Polizelli, M. A., Menegalli, F. C., Telis, V. R. N., & Telis-Romero, J. (2003). Friction losses in valves and fittings for power-law fluids. *Brazilian Journal of Chemical Engineering*, 20(4), 455–463. https://doi.org/10.1590/S0104-66322003000400012

Poole, R. J., & Ridley, B. S. (2007). Development-length requirements for fully developed laminar pipe flow of inelastic non-Newtonian liquids. *Journal of Fluids Engineering,* 1281-1287. https://doi.org/10.1115/1.2776969

Rohrig, R., Jakirlic, S., & Tropea, C. (2015). Comparative computational study of turbulent flow in a 90 deg pipe elbow, *International Journal of Heat Fluid Flow*, 55 (ETMM10), 102–111. https://doi.org/10.1016/j.ijheatfluidflow.2015.07.011

Rudman, M., Blackburn, H. M., Graham, L. J., & Pullum, L. (2004). Turbulent pipe flow of shear-thinning fluids. *Journal of Non-Newtonian Fluid Mechanics*, 118(1), 33-48. https://doi.org/10.1016/j.jnnfm.2004.02.006

Shapovalov, V. M. (2017). On the applicability of the Ostwald–de Waele model in solving applied problems. *Journal of Engineering Physics and Thermophysics*, 90(5), 1213-1218. https://doi.org/10.1007/s10891-017-1676-9

Shwin, S., Hamdani, A., Takahashi, H., & Kikura, H. (2017). Experimental investigation of two-dimensional velocity on the 90 double bend pipe flow using ultrasound technique. *World Journal of Mechanics*, 7(12), 340-359. https://doi.org/10.4236/wjm.2017.712026

Singh, V., Kumar, S., & Mohapatra, S. K. (2019). Modeling of erosion wear of sand water slurry flow through pipe bend using CFD. *Journal of Applied Fluid Mechanics*, 12(3), 679-687. https://doi.org/10.29252/jafm.12.03.29199

Straka, M., Eichler, T., Koglin, C., & Rose, J. (2019). Similarity of the asymmetric swirl generator and a double bend in the near-field range. *Flow Measurement and Instrumentation*, 70, 101647. https://doi.org/10.1016/j.flowmeasinst.2019.101647

Xiong, W., Kalkühler, K., & Merzkirch, W. (2003). Velocity and turbulence measurements downstream of flow conditioners. *Flow Measurement and Instrumentation*, 14(6), 249-260. https://doi.org/10.1016/S0955-5986(03)00031-1

Yigit, S., Graham, T., Poole, R. J., & Chakraborty, N. (2016). Numerical investigation of steady-state laminar natural convection of power-law fluids in square cross-sectioned cylindrical annular cavity with differentially-heated vertical walls. *International Journal of Numerical Methods for Heat & Fluid Flow*, 26 (1), 85-107. https://doi.org/10.1108/HFF-01-2015-0030

Yoon, K., Jung, H. W., & Chun, M. S. (2017). Secondary flow behavior of electrolytic viscous fluids with Bird-Carreau model in curved microchannels. *Rheologica Acta*, 56(11915-926. https://doi.org/10.1007/s00397-017-1033-0

Żelasko, J., & Niezgoda-Żelasko, B. (2010). Generalized non-Newtonian flow of ice slurry through bends. *Transactions of the Institute of Fluid-Flow Machinery* 45-60.